

Article

Modeling the Excess Velocity of Low-Viscous Taylor Droplets in Square Microchannels

Thorben Helmers ^{1,*} , Philip Kemper ² , Jorg Thöming ²  and Ulrich Mießner ¹ 

¹ Department of Environmental Process Engineering, University Bremen, Leobener Str. 6, 28359 Bremen, Germany

² Department of Chemical Process Engineering, University Bremen, Leobener Str. 6, 28359 Bremen, Germany

* Correspondence: helmers@uvt.uni-bremen.de; Tel.: +49-421-218-63337

Received: 18 July 2019; Accepted: 26 August 2019; Published: 2 September 2019



Abstract: Microscopic multiphase flows have gained broad interest due to their capability to transfer processes into new operational windows and achieving significant process intensification. However, the hydrodynamic behavior of Taylor droplets is not yet entirely understood. In this work, we introduce a model to determine the excess velocity of Taylor droplets in square microchannels. This velocity difference between the droplet and the total superficial velocity of the flow has a direct influence on the droplet residence time and is linked to the pressure drop. Since the droplet does not occupy the entire channel cross-section, it enables the continuous phase to bypass the droplet through the corners. A consideration of the continuity equation generally relates the excess velocity to the mean flow velocity. We base the quantification of the bypass flow on a correlation for the droplet cap deformation from its static shape. The cap deformation reveals the forces of the flowing liquids exerted onto the interface and allows estimating the local driving pressure gradient for the bypass flow. The characterizing parameters are identified as the bypass length, the wall film thickness, the viscosity ratio between both phases and the Ca number. The proposed model is adapted with a stochastic, metaheuristic optimization approach based on genetic algorithms. In addition, our model was successfully verified with high-speed camera measurements and published empirical data.

Keywords: Taylor flow; droplet excess velocity; droplet velocity model; microfluidics; genetic algorithms; greybox modeling

1. Introduction

Microscopic multiphase flows facilitate a wide field of possible applications since they provide short diffusion layers within the flow structures. This enables high mass and heat transfer rates [1,2] for several applications ranging from extraction [3] and multiphase catalyst reactions [4] to improved unit operations such as mixing tasks [5]. The distinct features allow performing reactions at new process windows with fewer hazards or higher selectivity [6]. The specific flow conditions can furthermore serve for cell isolation [7], genetic analysis [8] and reaction screening in a droplet chain [9]. In contrast to large scale multiphase flows, microscopic flows are much easier to predict as there are no complex interactions such as swarm turbulence [10,11] commonly found in bubble columns. In fact, the reproducibility of Taylor flows is a key for the application of microscopic multiphase flows [12].

In the Taylor flow regime, the disperse phase is separated from the wall by a thin wall film and does not fill the entire cross-section of the microchannel. The remaining space between the droplet and the microchannel's corners is occupied by the continuous phase, which is referred to as gutters [13]. The droplets are typically longer than the channel diameter, which leads to separated elongated disperse phase instances. The continuous phase segments between the droplets are called slugs. Taylor flows are mainly established in circular capillaries or rectangular microchannels whereas

especially the hydrodynamics of moving Taylor droplets in circular capillaries and the role of the thin wall film have been intensively studied [14].

Chemical reactions on the microscale are often performed in monolith reactors functioning as a catalyst support. In these reactors, a high number of parallelized channels with hexagonal or square channel cross-section offer a high specific reaction area for wall placed catalysts at small wall thickness. This results in a better heat transfer through the walls and better mechanical stability than circular capillaries [15]. For process control and stabilization, as well as precise reactor design, knowledge of the underlying fluidic terms is crucial. The high grade of parallelity complicates the prediction of the hydrodynamics and the resulting pressure drop [16,17].

Besides disperse phase size distribution and formation frequency [18], the actual droplet velocity is essential for the droplet residence time in the reactor. It determines the contact time of the educts and influences the pressure drop of the reactor [19]. In parallel reactors, the exact knowledge of the pressure drop is especially necessary since a steady educt supply for each individual single reactor is needed to ensure stable and efficient working conditions [20].

Several publications deal with the droplet velocity in rectangular capillaries and observe a droplet velocity mostly faster than the superficial velocity (see Section 3). For flows in circular capillaries, where only a thin wall film is present, this velocity difference is well understood [21], while for rectangular microchannels a variety of explanations exist, which mostly correlate the relations from measurements [22]. This complicates the transfer of results to other flow applications or altered process parameters since local and instantaneous hydrodynamic parameters are mostly not taken into account by the models and correlations.

This work aims to establish a model to determine the droplet velocity from the actual flow conditions [23]: e.g., droplet length, material properties, and the Ca number. In a first step, we develop a concept for the relative droplet velocity, which bases this velocity on extrinsic parameters, allowing a linear scaling. From this concept, we identify the bypass flow through the gutters as well as the film-thickness as the prominent parameters for the excess velocity.

In the next step, we develop a model that uses the local surface curvature of the gutters to retrieve the local pressure at the entrance and outlet of the gutter as a driving force. The bypassing gutter flow is calculated based on the counterplay of this driving force, the gutter length and a viscosity correlated resistance factor β . The local droplet curvature at the gutter entrances is derived with an analytical interface shape approximation [24] and a correlation for the droplet cap curvature based on the Ca number from our previous work [25]. The model was successfully validated using high-speed camera measurements.

2. Hydrodynamic Fundamentals of Taylor Flows

The Taylor flow regime in rectangular microchannels is mainly influenced by surface tension forces rather than inertia forces. In the Taylor flow regime, a droplet fills nearly the whole cross-section of a hydrodynamic channel, while the continuous phase occupies the gutters and a thin wall film. The droplets are divided by the slugs, consisting only of liquid from the continuous phase.

The interaction between interfacial and viscous forces is described by the Capillary number Ca .

$$Ca = \frac{u_0 \eta_c}{\sigma} \quad (1)$$

Herein, η_c represents the dynamic viscosity of the continuous phase, σ the interfacial tension between both phases and u_0 the total superficial flow velocity:

$$u_0 = \frac{Q_0}{A_{ch}} = \frac{Q_d + Q_c}{W \cdot H} = \frac{Q_d + Q_c}{H^2 \cdot ar} \quad (2)$$

The superficial velocity u_0 is based on the volume flow of the disperse Q_d and continuous Q_c phase as well as the microchannel's cross-sectional area A_{ch} that calculates from the channel width W and channel height H or, respectively, the channel aspect ratio $ar = \frac{W}{H}$.

For energetic considerations, knowledge of the ratio between inertia and viscous forces is of importance. The Reynolds number

$$Re = \frac{u_0 H \rho_c}{\eta_c} \quad (3)$$

is used to describe the ratio between inertia and viscous forces of the continuous phase with ρ_c being the continuous phase density and η_c the continuous phase viscosity. Additionally, the viscosity ratio

$$\lambda = \frac{\eta_d}{\eta_c} \quad (4)$$

between both phases has a significant influence on the pressure drop and the velocity of a droplet [19,26,27] since it indicates the momentum coupling into the disperse phase. Please note that the definition of λ differs in the mentioned publications.

Considering the overall classification of the applied flow system, the material properties of both fluid phases are of importance. The Ohnesorge number Oh describes the most prominent material properties for droplets being formed or dispersed [28]. It characterizes the fluidic system independent of current flow or forces and is mostly used when working with surfactants to manipulate the flow properties. Here, we use the Oh number to characterize the continuous phase.

$$Oh = \frac{\eta_c}{\sqrt{d \rho_c \sigma}} = \sqrt{\frac{Ca}{Re}} \quad (5)$$

In many applications, Taylor droplets in rectangular microchannels move with a velocity different from the superficial velocity, because the droplet does not fill the entire channel cross-section and continuous phase can bypass the droplet through the gutters. An early description was given by Wong et al. [29], who described these phenomena analytically and declared two possible regimes.

In the first regime, the fluid in the gutters moves slower than the droplet, dissipating kinetic energy. For the gutters, Abiev [21] reported an inverted pressure gradient, indicated by the local surface curvature. For circular microchannels, this results in an inverse flow of the wall film and the droplet moves faster than the superficial velocity.

In the second flow regime, which holds true for long and highly viscous droplets [27,29,30], more energy is dissipated through the larger wall film area and through viscous dissipation in the droplets. Consequently, the flow in the gutters moves from the droplet back to the front. Thus, the droplet moves slower than the superficial velocity.

For both regimes, the thin wall film resists the motion of the droplet, resulting in a difference in pressure with higher value at the back and a lower value at the front of the droplet. The transition between both regimes is described by a critical flow rate and depends on the droplet length and the channel aspect ratio [29].

Jakiela et al. [31] focused experimentally on the influence of the momentum coupling between both phases represented by λ and also revealed a dependence of the droplet velocity on the droplet length. For short, low viscous droplets ($\lambda < 1$), the droplets move faster than the superficial velocity and the droplet behavior is assigned to the first flow regime. Highly viscous droplets ($\lambda > 1$) move either faster or slower than the superficial velocity, depending strongly on the droplet length.

3. Concept of Excess Velocity

Based on the instantaneous droplet velocity u_d , which is evident and directly measurable via optical or electrical measurement techniques [32], different explanatory approaches for the deviation of superficial velocity u_0 and droplet velocity u_d have been reported.

Liu et al. [33] defined this relative difference as slipping velocity u_{slip} , Howard and Walsh [34] as relative drift velocity u_{drift} , Angeli and Gavrilidis [35] as relative bubble velocity u_{rel} and Abadie et al. [36] as dimensionless droplet velocity. Jakiela et al. [31] focused directly on the ratio of $\frac{u_d}{u_0}$ and named this quotient droplet mobility according to Bretherton [37]. For this work, we summarize these approaches as a slipping velocity:

$$u_{slip} = \frac{u_d - u_0}{u_d} = 1 - \frac{u_0}{u_d} \quad (6)$$

In those concepts, the desired quantity is scaled with an intrinsic value such as the instantaneous droplet velocity, which leads to normalization effects as values $u_{slip} < 1$ and $u_{slip} > 1$ are not normalized symmetrically (Figure 1). This behavior has to be taken into account when experimental or simulative data is interpreted.

In our approach, we scale the velocity difference with the superficial velocity as an extrinsic property and, staying in the terms of extrinsic denomination, define it as an excess velocity u_{ex}

$$u_{ex} = \frac{u_d - u_0}{u_0} = \frac{u_d}{u_0} - 1 \quad (7)$$

In this manner, u_{ex} results values around 0 for droplet velocities equal to the superficial velocity (plug flow), while positive and negative values indicate droplets that are, compared to the superficial velocity, faster or slower, respectively.

The advantage of this extrinsic concept stands out in a comparison of both approaches (Figure 1). The first shown intrinsic concept (slip velocity) leads to an asymmetrical scaling behavior, especially for droplets with $u_d < u_0$, since $u_{slip} < 0$ decreases more strongly than $u_{slip} > 0$ would increase. For applications such as balancing or process modeling, a linear behavior of ratio values is preferable to simplify the balances. Otherwise, the nonlinear behavior would lead to an additional bias towards any direction $u_d < u_0 \vee u_d > u_0$, which requires a nonlinearly compensation in the description of the phenomena and complicates the model development.

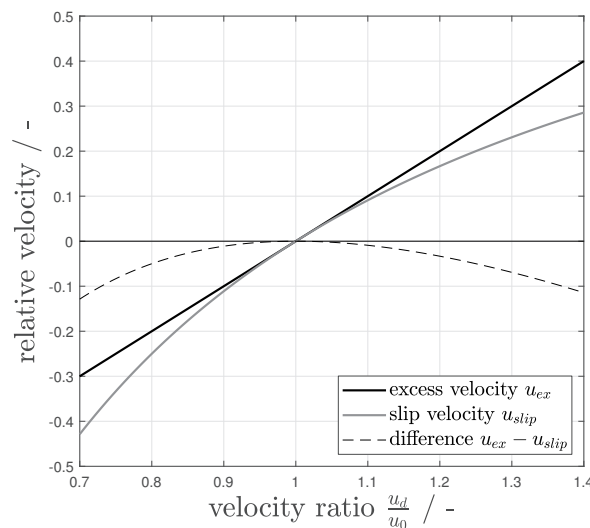


Figure 1. Comparison of different concepts of calculating the relative droplet velocity: excess velocity from this work (black solid line), slip velocity (grey solid line) and difference of both concepts (black dashed line).

A description for the excess velocity can be derived from the volume flows around moving droplets (Equation (8)). The continuity equation describes the connection between the gutter flow and the outer driving flows and delivers the relation between the total flow Q_0 and the volume flow fractions of the disperse Q_d as well as the continuous phase Q_c . Considering the unit cell of a single

slug and an adjoining droplet, the continuous phase divides into the volume flow of the slug (Q_s), the flow through the gutters (Q_g), and through the wall film (Q_f):

$$Q_0 = Q_d + Q_c = Q_d + (Q_s + Q_g + Q_f) \quad (8)$$

If we depict the flows at a moving Taylor droplet (Figure 2a) and introduce a stationary control surface Γ (Figure 2b), velocities can be retrieved from the balances, while two different flow states are possible: In the case of a droplet passing Γ , the slug volume flow through the control surface is $Q_s = 0$ (since there is no slug present). For a slug passing Γ , only the slug volume Q_s is present. As one can see, the use of a stationary point of view leads to nonstationary terms in the balances.

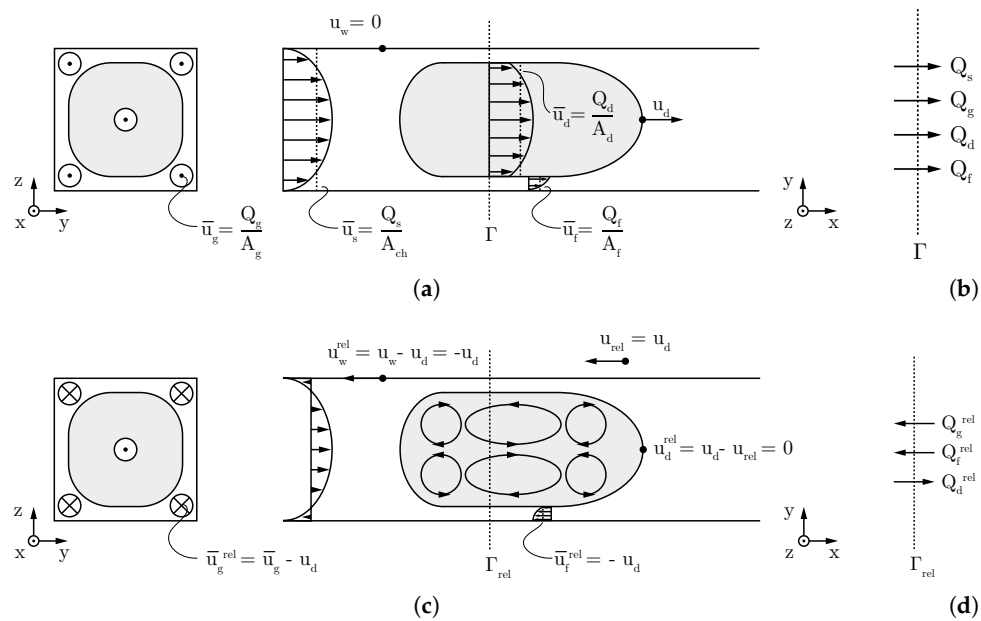


Figure 2. Prominent averaged and local velocity for a flowing droplet, where overlined entities represent area-averaged velocities. The film flow is not shown in this drawing. (a) Velocities for a fixed point-of-view (fixed frame); (b) flow balance at a steady control surface; (c) velocities for a moving point-of-view with the velocity u_d (moving frame); and (d) flow balance at a moving control surface.

If the coordinate system is changed from a fixed frame to a moving frame by moving the control surface with an arbitrary velocity u_{rel} , the balances become stationary and relative velocities become visible (Figure 2c). For this moving coordinate system, an additional volume flow Q_{rel} adds to the balances that result from the transformation of the coordinate system (Figure 2d):

$$Q_{rel} = u_{rel} \cdot A_{ch} \quad (9)$$

This changes Equation (8) to:

$$Q_0 - Q_{rel} = Q_d + Q_g + Q_f - Q_{rel} \quad (10)$$

With knowledge of the specific areas for each distinct volume flow rate, the averaged velocities can be calculated. Following Figure 3a,c, we conclude for the gutter area A_g of all four gutters

$$A_g = 4 \left[\left(\overline{R_g}^2 - \frac{\pi \overline{R_g}^2}{4} \right) + 2\delta \overline{R_g} + \delta^2 \right] \quad (11)$$

with δ denoting the wall film-thickness and $\overline{R_g}$ representing the mean dynamic gutter radius, which is described below in Section 4. For the cross-sectional film area A_f , we state with the aspect ratio $ar = WH^{-1}$

$$A_f = \frac{4\delta}{H} H^2 \left(\frac{1 + ar}{2} - 2 \frac{\overline{R_g} + \delta}{H} \right) \quad (12)$$

The droplet cross-sectional area A_d is delivered combining A_g and A_f :

$$A_d = A_{ch} - (A_g + A_f) \quad (13)$$

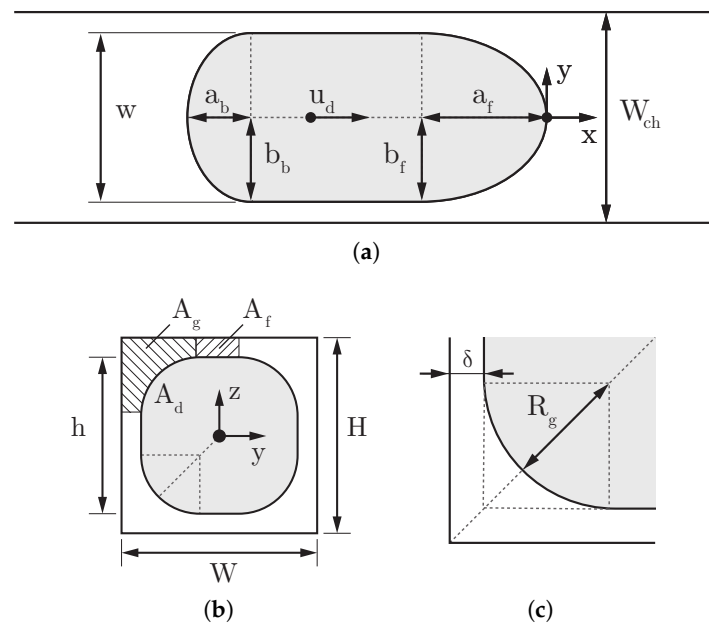


Figure 3. Declaration of relevant geometry for the model of a Taylor droplet flowing through a rectangular microchannel with the droplet velocity u_d . (a) Top-view of x-y-plane, characterizing the droplet with the front (a_f, b_f) and back cap (a_b, b_b), as well as the channel width W and droplet width w . (b) Droplet front-view in y-z-plane with the droplet area A_d , gutter area A_g , film area A_f , channel height H and the droplet height h . Only one representation of each area is shown. (c) Close-up of the droplet corner region with gutter radius (R_g) and the film-thickness δ .

With the cross-sectional areas of the droplet, the gutter and the wall film, the volume flow rates can be rearranged to area-averaged velocities and Equation (10) becomes

$$u_0 A_{ch} - u_{rel} A_{ch} = \overline{u_d} A_d + \overline{u_g} A_g + \overline{u_f} A_f - u_{rel} A_g - u_{rel} A_d - u_{rel} A_f \quad (14)$$

Herein, $\overline{u_d}$, $\overline{u_g}$ and $\overline{u_f}$ are area-averaged velocities of the droplet, gutter and film, respectively.

For the droplet ($Q_d = \overline{u_d} A_d - u_{rel} A_d$) and the film volume flow ($Q_f = \overline{u_f} A_f - u_{rel} A_f$), the transition velocity u_{rel} equals the stagnation point velocity u_d , since we assume incompressibility, mass conservation, a stagnant film and a stationary droplet shape [38].

$$\overline{u_d} = u_d \stackrel{!}{=} u_{rel} \quad (15)$$

Additionally, we assume the averaged velocity in the thin wall films to be insignificant for $Ca < 0.2$

$$\overline{u_f} \approx 0 \quad (16)$$

Therefore, Equation (14) simplifies to

$$(u_0 - u_d)A_{ch} = \overline{u_g^{rel}}A_g + (0 - u_d)A_f \quad (17)$$

Herein, $\overline{u_g^{rel}} = \overline{u_g} - u_d$ represents the relative gutter velocity, which dissipates flow energy in the gutter. Simplification and combination with Equation (7) leads to

$$\frac{u_d}{u_0} - 1 = u_{ex} = -\frac{\overline{u_g^{rel}}A_g}{u_0A_{ch}} + (u_{ex} + 1)\frac{A_f}{A_{ch}} \quad (18)$$

We neglect the terms that are small of higher-order (see Appendix A) and retrieve an expression for the excess velocity:

$$u_{ex} = -\frac{Q_g^{rel}}{Q_0} + \frac{A_f}{A_{ch}} \quad (19)$$

The relative gutter volume flow (Q_g^{rel}) and the cross-sectional area of the wall film A_f are the most prominent influencing quantities for the excess velocity. Thus, our proposed model aims to especially determine these quantities.

4. Model Specification

The considerations of the previous section identify the volume flows, which determine the excess velocity. In a second step, we clarify the relevant influential parameters on these volume flows and their interconnection.

For the proposed modeling approach, we adapt a greybox model following Hangos and Cameron [39]. Our model is developed from engineering principles, hydrodynamic considerations (see Section 3) and well-defined equations, whereas the initialization of a part of the influential parameters is based on measured data. The underlying relations can be described as an intermediate concept between a black box (completely based on measurement data) and a white box model (based only on analytically well-known equations and engineering principles).

As depicted in Section 3, we assume a droplet flowing through a rectangular microchannel with its properties according to Figure 3. The thin wall film cross-section A_f is determined by Equation (12) and depends on the channel height H , the channel aspect ratio ar and the film-thickness δ . To determine δ , we apply the model of Han and Shikazono [40], which holds for $Ca < 0.2$. For the proposed excess velocity model, full wettability of the walls with a stable wall film is assumed. Besides this behavior being proven in the later measurements (see Section 6), we compared this assumption with the literature. Kreutzer et al. [41] analytically retrieved the counterplay of film rupture in the region near the gutters and film formation at the bubble or droplet front. Furthermore, they found coherences for the length where the film starts to rupture. For short or fast droplets, new films are formed more quickly than they rupture. In this work, mainly short droplets are covered.

Khodaparast et al. [42] focused on the dewetting of the wall film and found a distance from the droplet front, at which dewetting occurs, to correlate with Ca in the range $10^{-5} \leq Ca \leq 10^{-2}$ and the surface wettability. As a criterion, they found a minimum film-thickness of 100 nm, beyond which rupture is suppressed. For the presented range of the model ($10^{-5} \leq Ca \leq 10^{-2}$, $0.5 \leq Re \leq 3$), based on the film thickness model of Han and Shikazono [40], the critical film-thickness never drops below this value.

For the flow of the bulk phase as well as the flow in the gutters, we omit the influence of viscous heating based on the criterion of Morini [43]. We elaborate on this in Appendix B.

The relative volume flow through the gutter Q_g^{rel} is derived from the pressure difference along the gutters, as suggested by Abiev [21]. Therefore, knowledge of the relevant pressures is crucial. It can be determined from the dynamic interface deformation caused by the moving liquids through the gutters in flow direction [44]. Stagnant droplets have a static cap shape with a circular outline according to

Musterd et al. [45]. When set into motion, the moving liquids exert forces onto the interface and cause a dynamic shape deformation [38].

A model proposed by Mießner et al. [24] allows to approximate the droplet shape and gutter diameter. The model implies that the deformation difference of the dynamic droplet cap shape between the droplet front and back results in a change of the gutter radius from the static shape. The cross-sectional gutter area A_g widens asymmetrically from back to front. The growing gutter radii accommodate the relative volume flow Q_g^{rel} of the continuous phase through the gutter. The gutter entrance at the droplet front is therefore larger than the gutter exit at the droplet back. Utilizing their model, the dimensionless radius of these gutters can be calculated from the flow-related curvature of the droplet.

The gutter radius $k_{g,i}$ is therefore defined as a fraction of the droplet height h . For the case of present wall films, the term is expressed as follows:

$$k_{g,i} = \frac{R_{g,i}}{h} = \frac{R_{g,i}}{H - 2\delta} \quad (20)$$

To simplify the geometry, we define a mean gutter radius \overline{R}_g using Equation (20):

$$\overline{R}_g = \frac{k_{g,f}(H - 2\delta) + k_{g,b}(H - 2\delta)}{2} \quad (21)$$

$$= \frac{(H - 2\delta)(k_{g,f} + k_{g,b})}{2} \quad (22)$$

which is also used for the mean cross-sectional area A_g derived with Equation (11).

In previous work [25], we introduced a quantification of the droplet cap deformation with an elliptic approximation of the cap outline

$$k_{c,f} = \frac{a_f}{b_f} \quad (23)$$

$$k_{c,b} = \frac{a_b}{b_b} \quad (24)$$

The ratio of the semi-major a and semi-minor axis b of the droplet cap curvature is introduced as deformation ratios $k_{c,i}$ at the droplet front and back. They become $k_{c,f} = k_{c,b} = 1$ when describing the static circular droplet cap shape of the droplet front and back. For the dynamic cap shape, under the influence of the moving liquids, the droplet front appears elongated $k_{c,f} > 1$ and the back cap is compressed in flow direction $k_{c,f} < 1$. Hence, we introduce a correlation to describe these relations: The cap curvature only depends on the Ca number for moderate flows ($Re < 5$):

$$k_{c,i} = m_{cap} \cdot Ca^{c_{cap}} + n_{cap} \quad (25)$$

With the correlation approach from our recent publication and the model from Mießner et al. [24], we are able to calculate the Laplace pressure at the gutters. We assume a linear connection between the gutter front and the back of the droplet body, since the curvature of the gutter in flow direction is negligibly small. In this case, the mean interface curvature at the gutter entrance and its exit depends on the gutter radii only, and the flow-induced Laplace pressure difference equals:

$$\Delta p_{g,f} = \sigma \left(\frac{1}{R_{g,f}^{stat}} - \frac{1}{R_{g,f}} \right) \quad (26)$$

$$\Delta p_{g,b} = \sigma \left(\frac{1}{R_{g,b}^{stat}} - \frac{1}{R_{g,b}} \right) \quad (27)$$

Those deformation related pressures at the droplet front and back provide a link to the driving pressure difference Δp_{LP} along the gutter length in the flow direction. Due to symmetry, the static terms cancel out:

$$\begin{aligned}\Delta p_{LP,fb} &= \Delta p_{g,f} - \Delta p_{g,b} \\ &= \sigma \left(\frac{1}{R_{g,f}} - \frac{1}{R_{g,b}} \right)\end{aligned}\quad (28)$$

Using the dimensionless expression from Equation (20), this results in

$$\Delta p_{LP,fb} = \sigma \left(\frac{1}{k_{g,f}(H-2\delta)} - \frac{1}{k_{g,b}(H-2\delta)} \right) \quad (29)$$

$$= \left(\frac{\sigma}{H} \right) \frac{1}{\left(1 - \frac{2\delta}{H}\right)} \left(\frac{k_{g,b} - k_{g,f}}{k_{g,f} \cdot k_{g,b}} \right) \quad (30)$$

for the flow-induced pressure difference as a driving force.

The relative volume flow rate through the four gutters Q_g^{rel} can be modeled as a laminar pressure driven flow [46] and it is linked to this pressure difference with a hydrodynamic resistance Ω :

$$Q_g^{rel} = \frac{1}{\Omega} \Delta p_{LP,fb} \quad (31)$$

The hydrodynamic resistance Ω was defined by Ransohoff and Radke [47] and Shams et al. [27] as

$$\frac{1}{\Omega} = \frac{\overline{R}_g^2}{\beta} \frac{A_g}{\eta_c l_g} \quad (32)$$

Besides the gutter length l_g , β denotes a dimensionless factor, which represents the geometrical obstructions of the gutter flow, as well as the viscous coupling of both flow phases. In accordance with the simulation results of Shams et al. [27], we declare an influence from the viscosity ratio λ of the flow phases to take care of the viscous coupling effects:

$$\beta = m_\beta \cdot \lambda^{c_\beta} + n_\beta \quad (33)$$

The gutter length l_g can be derived from the droplet length l_d , if the gutter distance $\Delta x_{g,i}$ from the caps is subtracted:

$$l_g = l_d - \Delta x_{g,f} - \Delta x_{g,b} \quad (34)$$

The gutter distance from the front and back droplet tip $\Delta x_{g,i}$ was defined by Mießner et al. [24] as

$$\Delta x_{g,i} = k_{c,i} \frac{H}{2} \left[\left(ar - \frac{2\delta}{H} \right) + \left(1 - \frac{2\delta}{H} \right) (1 - 2k_{g,i}) \right] \quad (35)$$

The above-stated considerations lead to our final description for the relative volume flow through the gutters

$$Q_g^{rel} = \frac{\overline{R}_g^2}{\beta} \frac{A_g}{\eta_c l_g} \Delta p_{LP,fb} \quad (36)$$

Herein, \overline{l}_g and Δp_{LP} depend on \overline{R}_g as the preceding considerations show. Thus, \overline{R}_g has the most prominent influence feature besides β . Inserting Equations (36) and (33) into Equation (19) delivers

$$u_{ex} - \frac{A_f}{A_{ch}} = \frac{1}{Ca} \frac{1}{\beta} \frac{\overline{A}_g}{A_{ch}} \frac{\overline{R}_g^2}{l_g H} \frac{1}{(1 - \frac{2\delta}{H})} \left(\frac{k_{g,b} - k_{g,f}}{k_{g,f} \cdot k_{g,b}} \right) \quad (37)$$

expanding with $\frac{W}{W}$ and inserting l_g (Equation (34)), we receive our final expression for the excess velocity:

$$u_{ex} = \frac{1}{Ca} \frac{1}{\beta} \frac{W}{l_d} \frac{\overline{A}_g}{A_{ch}} \frac{\overline{R}_g^2}{\left(1 - \frac{\Delta x_{g,f}}{l_d} - \frac{\Delta x_{g,b}}{l_d}\right)} \frac{1}{A_{ch} \left(1 - \frac{2\delta}{H}\right)} \left(\frac{k_{g,b} - k_{g,f}}{k_{g,f} \cdot k_{g,b}} \right) + \frac{A_f}{A_{ch}} \quad (38)$$

We point out that our model is usable within the capillary regime $Ca < 0.02$ since the model for the wall film-thickness from Han and Shikazono [40], the analytic interface model from Mießner et al. [24] and the droplet curvature correlation from our recent work [25] are valid in this range. At higher Ca in the viscous regime, different flow conditions with thicker wall films [22] as well as a higher influence of Re are reported [48].

5. Model Calibration

The final expression for the excess velocity (Equation (38)) depends on accessible data such as W , ar and l_d as well as on \overline{R}_g , β , $k_{g,f}$, $k_{g,b}$, $\Delta x_{g,f}$ and $\Delta x_{g,b}$, whereas the latter is also related to the gutter radii \overline{R}_g . As shown in the previous section, the parameters can be calculated from the droplet cap curvatures $k_{c,f}$ and $k_{c,b}$ and via measurement-based model calibration. The six parameters ($m_{cap,f}$, $m_{cap,b}$, $n_{cap,f}$, $n_{cap,b}$, $c_{cap,f}$, and $c_{cap,b}$) influencing the cap deformation at the droplet front and back as well as the dimensionless resistance factor β with m_β , c_β and n_β need to be adjusted.

For model calibration, we used the dataset presented in [25] in combination with supplementary measurements in the data range of low Ca and redefine n_{cap} within an interval around 1. Nevertheless, for $Ca \rightarrow 0$, it represents the point of minimal surface energy and equates a spherical droplet shape. This approach allows improving the convergence of solvers. Out of further a priori considerations ($\beta > 0$, $n_{c,f} \approx 1$), we additionally defined the boundaries for the search space of the solver presented in Table 1 and allowed the solver to adapt the correlation coefficients from our last work to the presented model and acquired measurement data.

Table 1. Boundaries of input values for optimization.

Parameter	Lower Boundary	Upper Boundary
$m_{cap,f}$	1.00	9.90
$c_{cap,f}$	0.40	1.50
$n_{cap,f}$	1.00	1.005
$m_{cap,b}$	−2.50	−1.00
$c_{cap,b}$	0.30	0.75
$n_{cap,b}$	0.995	1.00
m_β	0.00	10.00
c_β	0.50	1.5
n_β	0.50	20

Besides the fixed boundaries of the search space, a hydrodynamic boundary condition was applied to improve the convergence of the used optimization algorithms. For a rising Ca , the difference between $k_{g,f}$ and $k_{g,b}$ must increase, because of the pressure difference between the droplet front and back increases with higher Ca [21] and the droplet front elongates, which leads to a larger front gutter radius, while the droplet rear flattens out. This is expressed by the gutter radius increase for an increasing Ca :

$$\frac{dk_{g,f}}{dCa} > \frac{dk_{g,b}}{dCa} \quad (39)$$

The large number of influence parameters leads to a highly nonlinear optimization problem with numerous local minima. Thus, most gradient-based algorithms are not suitable for this type of optimization problem, which tend to converge to local optima. This would result in an enormous number of randomly initialized solver calls to cover the whole search space. In contrast, stochastic and metaheuristic approaches cover the search space to solve the statistical part of the greybox model by finding the global optimum.

The quality of a solver result (e.g., deviation between measured data and estimation) is quantified by the loss-function of the problem. For the model calibration, we define

$$\mathcal{L} = \omega_1 \left(\sum \frac{|k_{c,b} - k_{c,b}^{\mathcal{M}}|}{k_{c,b}^{\mathcal{M}}} + \sum \frac{|k_{c,f} - k_{c,f}^{\mathcal{M}}|}{k_{c,f}^{\mathcal{M}}} \right) + \omega_2 \sum \frac{|u_d - u_d^{\mathcal{M}}|}{u_d^{\mathcal{M}}} + \omega_3 \sum \frac{|\psi - \psi^{\mathcal{M}}|}{\psi^{\mathcal{M}}} \quad (40)$$

with the weights of the individual properties $\omega_1, \omega_2, \omega_3$ following Table 2. Values with an upper index \mathcal{M} denote values estimated by the model and values without an upper index represent the calibration data. The first two sums serve as calibration datasets for the hydrodynamic flow properties, since they contain the flow related deformation and therefore the hydrodynamic influences. The differences of the velocity u_d serves as a parameter for the actual droplet velocity and therefore the flow resistance β . This is necessary, since otherwise no representation for β is available.

Table 2. Weight factors ω_i of the loss-function for GA optimization.

ω_1	ω_2	ω_3
3.0	5.0	3.7

In addition, the concept of an equilibrium function ψ is introduced to maintain the overall integrity of the model: The excess velocity depends on extrinsic measurable values such as the dimensionless quantities and geometrical properties as well as varying flow properties such as the gutter length. Thus, it is appropriate to separate the measurable quantities from the model based quantities. In doing so, one can directly compare the quantities received from our correlation with measurement data adjusted for material and flow properties. The separation of those terms leads to the equilibrium function ψ (Equations (41) and (42)). Herein, Equation (41) represents the data from our measurements and Equation (42) only data from our modeling assumptions and geometry. For a well-adjusted model, the measured data for ψ (Equation (41)) should systematically correspond with the modeled values for ψ (Equation (42)).

$$\psi = \left(u_{ex} - \frac{A_f}{A_{ch}} \right) Ca \beta \frac{l_d}{W} \quad (41)$$

$$\psi^{\mathcal{M}} = \frac{\overline{A_g}}{A_{ch}} \frac{\overline{R_g}^2}{\left(1 - \frac{\Delta x_{g,f}}{l_d} - \frac{\Delta x_{g,b}}{l_d} \right)} \frac{1}{A_{ch} \left(1 - \frac{2\delta}{H} \right)} \left(\frac{k_{g,b} - k_{g,f}}{k_{g,f} \cdot k_{g,b}} \right) \quad (42)$$

The calibration procedure is based on a Genetic Algorithm (GA). For good optimization results, it is necessary to emulate a sufficiently sized genome pool, thus a high number of emulated individuals is preferred. This in turn results in a massively increased calculation demand, because, for each iteration step, every single individual and their children need to be evaluated [49]. Additionally, the genetic algorithm is typically performed iteratively to identify local optima. To decrease the number of time-consuming iteration steps of the GA and thereby reduce overall calculation time, we utilize a three-step stochastic and gradient-free approach.

In the first step, a random population at the feasible borders of the problem is generated for the Genetic Algorithm and a genetic optimization performed. The convergence point of the GA is initialized via Latin Hypercube Sampling processed by a following fast-converging Pattern

Search Algorithm (PSA) [50] that results in an improved minimum as the final convergence point. The properties of both algorithms are shown in Table 3. The algorithm finally merges at the values shown in Table 4. The results are discussed in the following.

Table 3. Properties of used solver algorithms.

Genetic Algorithm	
population size	200 individuals
creation function	random feasible population
scaling function	ranking
selection function	stochastic uniform
mutation function	adaptive feasible
crossover function	scattered
Pattern Search Algorithm	
search method	Latin Hypercube
poll method	complete poll

Table 4. Values for the fit-functions for droplet shape k_i and resistance β .

Target Value	m_i	c_i	n_i
k_f	4.8761	0.7465	1.0021
k_b	−1.6967	0.4745	0.9980
β	6.1280	1.2105	1.4541

For the flow-induced cap curvature, the solver merges to an exponential behavior as a function of the Ca number for both cap deformation ratios k_f and k_b , which coincides with the results of our previous works [24,25,51]. The retrieved correlation with underlying data points is shown in the Appendix (Figure A2). Our additional boundary condition (Equation (39)) is satisfied for all values as the graphs for the gutter radii $k_{g,i}$ show.

For the resistance factor β , no fitting data are available since it cannot be measured directly. Therefore, β is fitted based on the velocity data from high-speed camera measurements and the application of parameters for the droplet deformation (measurements are performed in the experimental setup described in [25]). The resulting droplet velocities in comparison with the measured values are shown in Figure 4. The measurements fit reasonably well in the range of inevitable velocity fluctuations caused by Taylor flow stability of $\pm 10\%$ range described by [13].

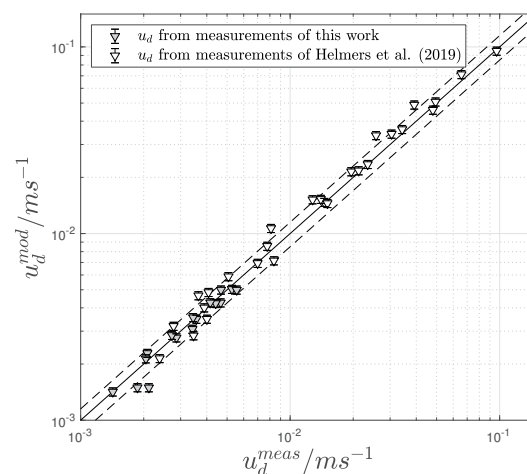


Figure 4. Parity plot for the droplet velocity of measured droplets and corresponding data from our model after adaption of the dimensionless resistance factor β . The values situate fairly good into the fluctuation range of 10%, as reported by van Steijn et al. [13], Fuerstman et al. [52].

6. Model Validation

For a first validation step, the equilibrium functions ψ and ψ^M are considered. In the case of a hydrodynamic well-adjusted model, both functions should coincide, and our model based shape deviations (ψ^M) equal the combination of measured properties (ψ). The corresponding data and the values for our model agree well at high Ca numbers (Figure 5), whereas a deviation for lower Ca numbers can be observed. This can be explained by the fact that the excess velocity itself is a relative quantity and it is strongly influenced at lower absolute values (low Ca number). Thus, an inevitable constant measurement deviation for velocity and volume flows caused by the experimental equipment results in a higher error for low excess velocities. Especially for $Ca < 10^{-4}$, the resulting volume flows are situated at $Q_0 \approx 2 \times 10^{-6}$ L/min and even minor deviations lead to high errors for the excess velocity. Thus, we consider our model approach to represent the measurements reasonably well and our fit coefficients to be valid.

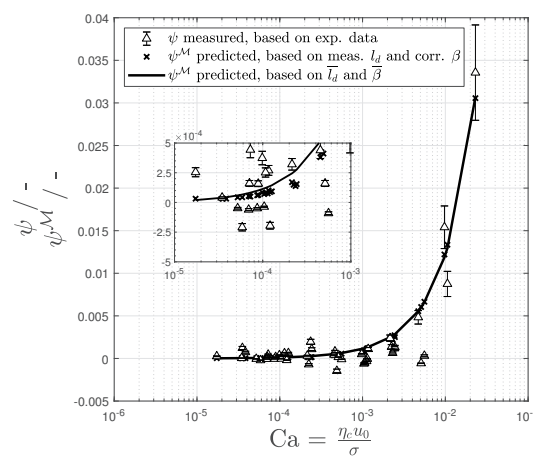


Figure 5. Calibration function ψ for measured (triangles) and modeled data ψ^M for the measured droplet lengths l_d and correlated β (crosses) over the Ca number. The black solid line depicts the calibration function for an averaged \bar{l}_d and $\bar{\beta}$ to clarify the underlying systematic.

Besides the hydrodynamic validation, our assumptions for β are compared with available simulation data. We found a dependence of the gutter flow resistance β on the viscosity ratio λ . The latter can be interpreted as an indicator for the viscous coupling of both flow phases (Figure 6). In the case of a highly viscous continuous phase ($\lambda < 1$), the strongest velocity gradients are found inside the droplet, while, for a viscous disperse phase ($\lambda > 1$), larger velocity gradients and therefore energy dissipation are found inside the gutter-flow, resulting in a larger β .

This approach agrees with the simulations from Shams et al. [27], who improved the model of Ransohoff and Radke [47] by introducing the viscous coupling of the disperse and the continuous phase. For our case of $0.1 \leq \lambda \leq 1.4$ and a contact angle $\theta = 0^\circ$, Shams et al. [27] reported a β of 20–30 for a co-current flow. Our values are shifted by a constant offset, while the slope and therefore the dependence on λ is similar. We consider the difference in the offset to be caused by the use of a different flow field specifications. Shams et al. [27] described a concurrent flow in a fixed frame specification, while in this work we determine Q_g^{rel} within a moving frame flow specification. The coordinate transformation only changes the offset of the function, while the hydrodynamic influence (the slope) must remain identical. Additionally, within the simulation of [27], they assumed a contact line between disperse phase, continuous phase and the wall in their problem definition. Although for the solution shown in Figure 6 the contact angle for the continuous phase is nearly 180° , the existence of a contact line introduces an additional resistance. Thus, regarding β , we consider our model plausible.

Due to the mentioned experimental restrictions, we cannot directly compare the modeled and experimental determined excess velocities u_{ex} . Instead, we compared the results of our model to different published approaches. A suitable correlation for the prediction of the excess velocity in the

first regime was introduced by Jose and Cubaud [22], who identified the Ca number and the ratio of the droplet length $\frac{l_d}{H}$ as characteristic properties (Figure 7). It has to be mentioned that the model of Jose and Cubaud [22] for non-wetting droplets ends at $\frac{l_d}{H} Ca^{-1} > 600$, since for larger values they observed the disperse phase to wet the channel walls. This results in intensified dissipation and a higher pressure drop and thereby inhibits a gutter flow from the droplet front to the back. This phenomenologically equals the second flow regime, as mentioned by Wong et al. [5], but lacks the thin wall film and results in a much larger pressure drop. Furthermore, the viscosity ratio λ is not included in their correlation.

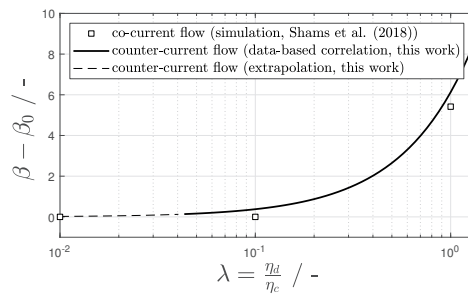


Figure 6. Comparison of calculated resistance factor β (squares) and correlation (solid and dashed line) of our model. The data of the simulation from Shams et al. [27] is shown as squares. Both datasets are corrected by the offset β_0 to compensate for the influence of the flow form (co-current or counter-current).

A comparison of our greybox model with the correlation from Jose and Cubaud [22] (Figure 7) shows good agreement. At very low Ca numbers ($Ca < 10^{-4}$), our model results in a slightly increased excess velocity. We regard this behavior of the model as not physical. The effect results from the mathematical counterplay of the terms $\lim_{Ca \rightarrow 0} \frac{1}{Ca} = \infty \leftrightarrow \lim_{Ca \rightarrow 0} k_{g,f} - k_{g,b} = 0$ within Equation (38). To achieve a stable solver convergence, we accepted a small residual deviation for the static case $Ca \rightarrow 0$ for the front and back shape of 0.1%. Due to the relative character of the excess velocity, this unfolds a significant influence at low Ca values. Unfortunately, additional measurement validation concerning the shape deviation at very low Ca is not possible in our experimental design, since the expected shape deviation is smaller than the blurriness of the interfacial area in the images itself and therefore lies inside the measurement deviation.

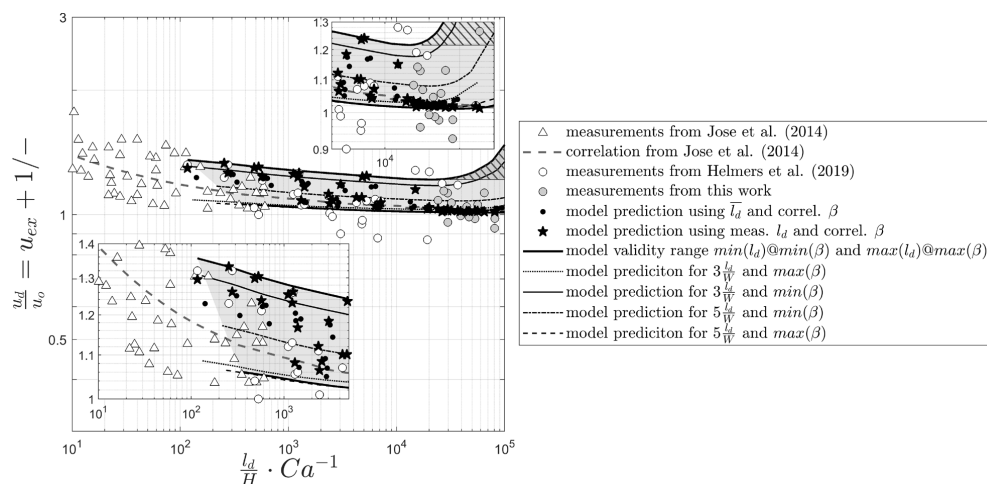


Figure 7. Comparison of our model (stars) and measurements (circles) with the measurements (triangles) and correlation from Jose and Cubaud [22] for a Taylor droplet in co-flow (axis scaling and normalization kept for comparability). The inclination for low Ca numbers (hatched area) is discussed in the text. Since the influence of l_d correlates linearly with Δp_{LP} instead of Ca in our model and β is not included in the x-axis normalization, we additionally show the borders of our model for the minimum/maximum l_d and β of our measurements.

7. Discussion

The interfacial area of a Taylor droplet in rectangular channels can be divided into the front and back cap regions, the wall films and the gutter interface. Neglecting the caps, the main momentum input into a droplet is transferred across the wall film and the gutter interface area. An increasing channel aspect ratio and droplet length result in a growing wall film area, i.e., an enlarged dissipation interface.

As shown in Section 2, the behavior of the Taylor droplet's excess velocity can be parted in two possible regimes and the viscosity ratio λ has a strong influence on the hydrodynamic mechanisms. In the first regime, the fluid in the gutter flows slower than the droplet, exerting a drag force and leading to a positive excess velocity $u_{ex} > 0$. These drag forces influence the droplet shape, leading to a flattened droplet back and elongated droplet front. We characterize this shape variation with a correlation (Section 5). As can be seen from the measurements, our data fall into this flow regime, as our resulting droplet shape indicates in accordance with Wong et al. [29].

The influence of the droplet length in the plug flow regime and $\lambda < 1$, where larger droplets have an $u_{ex} \approx 0$, is in agreement with Jakiela et al. [31] and their later publication [53]. Additionally, they found an elongation of the dynamic droplet length in comparison to the static droplet length, which is also covered by our shape correlation, since for rising the Ca number the droplet front elongates stronger than the droplet back is compressed. Recently published simulations by Kumari et al. [54] show that also for larger Re numbers $u_{ex} \approx 0$.

Our concept of deriving the excess velocity from the gutter pressure drop that is directed against the flow direction (larger pressure at the front gutter entrance) is in accordance with Abiev [21]. Nevertheless, the averaged pressure is still higher at the droplet back than at the droplet front due to the overall droplet pressure drop, since the droplet needs a driving force for its translation.

For the second flow regime identified by Wong et al. [29], where the viscous dissipation in the film and droplet leads to a bypass flow from the droplet back to the front and therefore a negative droplet excess velocity (for large λ and long droplets), our model can be adapted, if the gutter-shape-difference term is revised or a resistance coefficient for the film is added. As the viscosity ratio λ rises, more momentum will be dissipated via the wall films. This extra momentum is dissipated at the gutter interface, which results in a slower droplet velocity, forcing the continuous phase to bypass the droplet reversely. As the hydrophilized channels walls in our experimental setup did not allow establishing a water-in-oil two-phase flow with a $\lambda \gg 1$, droplet shape correlations, as well as measurements of u_{ex} for the case of $\lambda \gg 1$ should be performed in future work. Although we assume a systematic inversion of the gutter radii ratio back to front as a consequence of the reversed gutter flow direction, it should be mentioned that, with the current shape correlation, our model only works for the case of low viscous disperse phase ($\lambda \lesssim 1$) such as gas/liquid or low viscous oil/water flows.

The influence of the channel aspect ratio, as mentioned by Wong et al. [5], is incorporated in our model: a higher aspect ratio results in lower excess velocities. This can be explained by the larger drag forces acting on a larger relative wall film area caused by the flattened channel geometry.

8. Conclusions

In this work, we developed a model to determine the relative droplet velocity of Taylor flows in square microchannels for moderate Ca numbers and low to moderate viscosity disperse phase ($\lambda \lesssim 1$). We base our model on the relative volume flow through the gutters, as well as the wall film-thickness. The flow through the gutters is determined from the pressure drop described by the Laplace pressure difference between the gutter entrances.

Our model uses the gutter radii to obtain the resulting pressure gradient that drives the continuous phase through the gutters. We used measurements at different Ca and Re in a surfactant-free fluid system from a previous publication [25] to derive the radii at the gutter entrances from the surface shape model proposed by Mießner et al. [24] and calibrate the model parameters.

Our model was successfully validated with an intrinsic approach comparing the congruence of measurement data and calibrated model parameters. Additionally, we successfully compared our model to the phenomenological correlation of Jose and Cubaud [22].

The comparison with the most prominent approaches shows that our model and the chosen influential parameters are valid for moderate and small viscosity ratios. The excess velocity is determined by viscous dissipation in the droplet and the gutters as well as the drag of the thin wall films. The relation is characterized by the Ca number, the viscosity-ratio λ , the dimensionless gutter-length l_g , the aspect ratio ar and the wall film area A_f . Furthermore, the proposed model can close the gap for $\frac{l_d}{H}Ca^{-1} > 600$ and allows the calculation of the excess velocity for moderate Ca numbers ($Ca < 0.02$).

In the future, the influence of surfactants and highly viscous droplets ($\lambda \gg 1$) on the excess velocity should be investigated to extend the model, since an excess velocity $u_{ex} < 1$ has not been included into the model so far. We suggest to include this function in the modeling of the wall film resistance. Especially local spatially resolved measurement techniques, e.g., μ PIV measurements, should be appropriate for this task.

Author Contributions: Conceptualization, T.H. and U.M.; methodology, T.H., J.T. and U.M.; software, T.H., P.K. and U.M.; validation, T.H.; formal analysis, T.H. and U.M.; investigation, T.H.; resources, T.H.; data curation, T.H.; writing—original draft preparation, T.H.; writing—review and editing, U.M. and J.T.; visualization, T.H. and P.K.; and supervision, U.M. and J.T.

Funding: The contribution of P. Kemper has been supported by the German Research Foundation (DFG), Priority Program: "Reactive Bubbly Flows", SPP1740. The author gratefully acknowledges the financial support.

Conflicts of Interest: The authors declare no conflict of interest.

Abbreviations

The following abbreviations are used in this manuscript:

Acronyms/Abbreviations

GA	Genetic Algorithm
PIV	Particle Image Velocimetry
PSA	Pattern Search Algorithm

Dimensionless Quantities

λ	Viscosity ratio [–]
Ca	Capillary number [–]
Oh	Ohnesorge number [–]
Re	Reynolds number [–]

Greek Symbols

β	geometric coefficient of resistance [–]
δ	wall film-thickness [μm]
η	dynamic viscosity [$\text{Pa} \cdot \text{s}$]
Γ	control surface [–]
Ω	flow resistance [$\text{Pa} \cdot \text{s} \cdot \text{m}^{-3}$]
ω	weight factor [–]
ψ	dimensionless equilibrium function [–]
ρ	density [$\text{kg} \cdot \text{m}^{-3}$]
σ	interfacial tension [$\text{N} \cdot \text{m}^{-1}$]

Roman Symbols

A	cross-sectional area [μm^2]
a	semi-minor axis of ellipse [μm]
ar	aspect ratio [–]
b	semi-major axis of ellipse [μm]
c	fitting coefficient [–]
D	hydraulic diameter [μm]

d	characteristic length [m]
H	channel height [μm]
h	droplet height [μm]
k	dimensionless ratio [–]
l	length [μm]
m	fitting coefficient [–]
n	fitting coefficient [–]
Q	volume flow rate [$\mu\text{l} \cdot \text{min}^{-1}$]
R	radius [μm]
u	velocity [$\text{mm} \cdot \text{s}^{-1}$]
W	channel width [μm]
x	cap length till gutter entrance [μm]

Superscripts

\mathcal{M}	model calibration data
$meas$	measurement data
mod	model results
rel	relative
$stat$	stationary

Subscripts

0	superficial/total/offset
β	concerning resistance factor
c	continuous phase
c, b	back droplet cap
c, f	front droplet cap
c, i	front or back droplet cap
cap	concerning droplet cap curvature
ch	channel
d	disperse/droplet phase
ex	excess scale concept
f	wall film
fb	from front to back
g	gutter
g, b	gutter at back of droplet
g, f	gutter at front of droplet
g, i	i-th droplet gutter
LP	Laplace pressure
$mean$	arithmetic mean
rel	relative value
s	slug
$slip$	slipping scale concept

Other Symbols

$\overline{\quad}$	averaged value
--------------------	----------------

Appendix A. Considerations for Mixed Terms

For consideration of the mixed terms in u_{ex} , rearranging Equation (18) leads to the equation

$$u_{ex} - u_{ex} \frac{A_f}{A_{ch}} = \frac{Q_g^{rel}}{Q_0} + \frac{A_f}{A_{ch}} \quad (\text{A1})$$

Our measurements show in agreement with Jose and Cubaud [22] excess velocities with values $u_{ex} < 0.4$ for $Ca < 0.2$. Additionally, we can assume $\frac{A_f}{A_{ch}} < 0.005$, as shown in Figure A1. Thus, one can say $u_{ex} \frac{A_f}{A_{ch}} < 0.002$ and therefore it can be considered small of higher order and can be neglected.

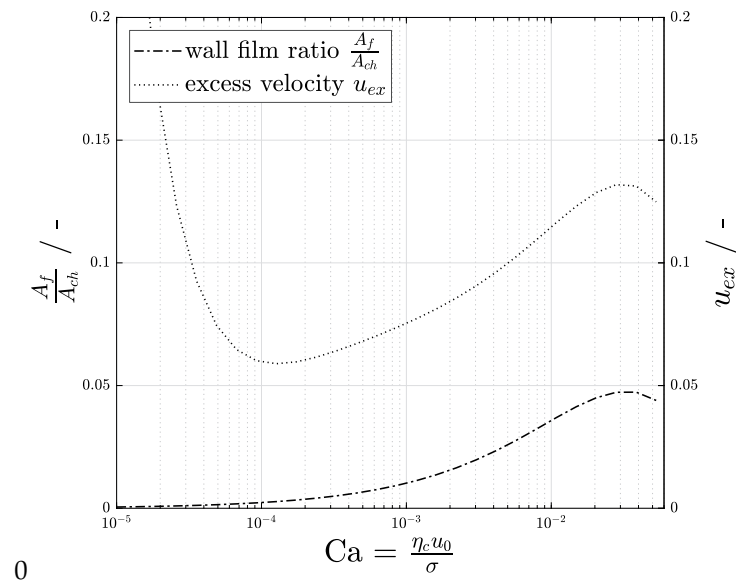


Figure A1. Dimensionless film-area and excess velocity for $\frac{l_d}{W} = 3$ and $\beta = 3.892$ for the proposed model.

The correlations, which were retrieved via a GA (Section 5), show a good agreement with the measurement data for the cap curvature from our last work and available literature data (Figure A2). Rising viscous forces indicated by a rising Ca number deform the droplet interface more strongly. At static conditions ($Ca \rightarrow 0$), the cap curvatures are in correspondence with Musterd et al. [45] roughly circular ($k_{c,f} = k_{c,b} \approx 1$). The back cap is compressed with respect to the main flow direction ($k_{c,b} < 1$) and the front cap elongated ($k_{c,f} > 1$) if viscous forces rise in comparison to the static case.

The size of the gutter radii rises with the increasing influence of the viscous forces, since the bypass flow in the gutter increases and needs to be accommodated by the gutters. The gutter entrance is always larger in diameter than the exit radius ($k_{g,f} > k_{g,b}$).

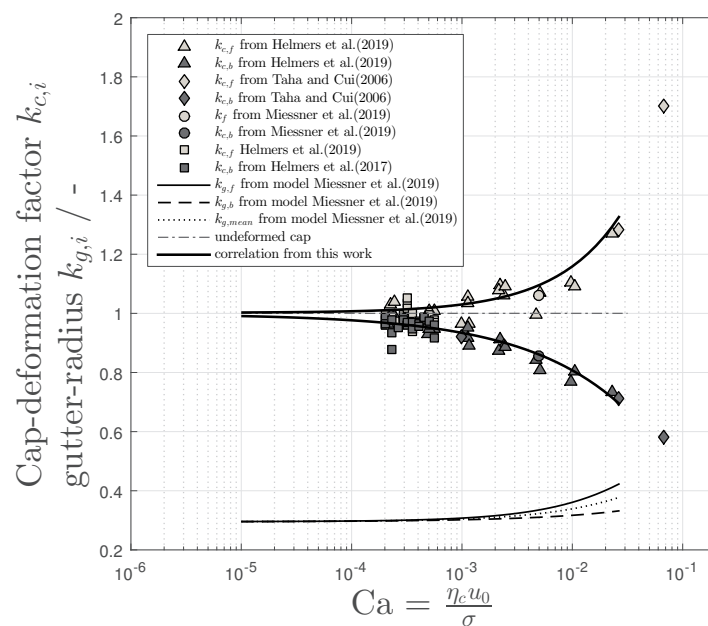


Figure A2. Measured values and retrieved correlation for the droplet cap deformation ratios $k_{c,f}$ and $k_{c,b}$ for different Ca numbers used in the proposed model. Additionally, the calculated dimensionless gutter-radii $k_{g,f}$, $k_{g,b}$ based on the model of Miessner et al. [24] are shown.

Appendix B. Criterion for Neglecting the Viscous Heating

Especially for microfluidic applications, flow phenomena such as viscous dissipation gain importance at specific scaling effects. Emerging from the energy dissipation, the temperature of the fluids can change (viscous heating) [55], as can relevant flow properties such as the viscosity change. To elaborate whether the viscous heating should be taken into account for the model, Morini [43] introduced a criterion, suggesting a bulk phase temperature increase of 1 °C as acceptable to still consider the viscosity unchanged. For adiabatic channels, they provided information of the critical Re depending on the hydraulic diameter. For $d_{hyd} = 200 \mu\text{m}$ and rectangular channels, they stated $Re \approx 1000$.

Considering the validity range of the proposed model for Ca and H , this critical Re is reached under no circumstances using u_0 and A_{ch} from our measurements as properties.

When focusing on the gutters instead, local Re of

$$Re_g = \frac{\frac{Q_0}{A_g} D_g \rho_c}{\eta_c} < 16 \quad (\text{A2})$$

are reached, if all four gutters are considered as one area equivalent circular tube with the diameter

$$D_g = \sqrt{4 \frac{A_g}{\pi}} \quad (\text{A3})$$

In addition, these maximum values of $Re_g \approx 16$ lie below the critical $Re_c \approx 1000$ following Morini [43] for circular microchannels. Thus, we consider it valid to neglect the viscous heating in the applied range of Ca and Re of the proposed model.

References

- Haase, S.; Murzin, D.Y.; Salmi, T. Review on hydrodynamics and mass transfer in minichannel wall reactors with gas–liquid Taylor flow. *Chem. Eng. Res. Des.* **2016**, *113*, 304–329. [\[CrossRef\]](#)
- Sattari-Najafabadi, M.; Nasr Esfahany, M.; Wu, Z.; Sunden, B. Mass transfer between phases in microchannels: A review. *Chem. Eng. Process. Process Intensif.* **2018**, *127*, 213–237. [\[CrossRef\]](#)
- Kralj, J.G.; Sahoo, H.R.; Jensen, K.F. Integrated continuous microfluidic liquid-liquid extraction. *Lab Chip* **2007**, *7*, 256–263. [\[CrossRef\]](#) [\[PubMed\]](#)
- Kobayashi, J.; Mori, Y.; Kobayashi, S. Multiphase organic synthesis in microchannel reactors. *Chem. Asian J.* **2006**, *1*, 22–35. [\[CrossRef\]](#) [\[PubMed\]](#)
- Wong, S.; Ward, M.; Wharton, C. Micro T-mixer as a rapid mixing micromixer. *Sens. Actuators B Chem.* **2004**, *100*, 359–379. [\[CrossRef\]](#)
- Sun, B.; Jiang, J.; Shi, N.; Xu, W. Application of microfluidics technology in chemical engineering for enhanced safety. *Process Saf. Prog.* **2016**, *35*, 365–373. [\[CrossRef\]](#)
- Chen, Y.; Li, P.; Huang, P.H.; Xie, Y.; Mai, J.D.; Wang, L.; Nguyen, N.T.; Huang, T.J. Rare cell isolation and analysis in microfluidics. *Lab Chip* **2014**, *14*, 626–645. [\[CrossRef\]](#)
- Hosokawa, M.; Nishikawa, Y.; Kogawa, M.; Takeyama, H. Massively parallel whole genome amplification for single-cell sequencing using droplet microfluidics. *Sci. Rep.* **2017**, *7*, 5199. [\[CrossRef\]](#)
- Jin, S.H.; Jung, J.H.; Jeong, S.G.; Kim, J.; Park, T.J.; Lee, C.S. Microfluidic dual loops reactor for conducting a multistep reaction. *Front. Chem. Sci. Eng.* **2018**, *12*, 239–246. [\[CrossRef\]](#)
- Kück, U.D.; Mießner, U.; Aydin, M.; Thöming, J. Mixing time and mass transfer of rising bubbles in swarm turbulence. *Chem. Eng. Sci.* **2018**, *187*, 367–376. [\[CrossRef\]](#)
- Mießner, U.; Kück, U.D.; Haase, K.; Kähler, C.J.; Fritsching, U.; Thöming, J. Experimental Assessment of an Innovative Device to Mimic Bubble Swarm Turbulence. *Chem. Eng. Technol.* **2017**, *40*, 1466–1474. [\[CrossRef\]](#)
- Kreutzer, M.T.; Kapteijn, F.; Moulijn, J.A.; Heiszwolf, J.J. Multiphase monolith reactors: Chemical reaction engineering of segmented flow in microchannels. *Chem. Eng. Sci.* **2005**, *60*, 5895–5916. [\[CrossRef\]](#)

13. Van Steijn, V.; Kreutzer, M.; Kleijn, C. Velocity fluctuations of segmented flow in microchannels. *Chem. Eng. J.* **2008**, *135*, S159–S165. [\[CrossRef\]](#)
14. Abiev, R.; Svetlov, S.; Haase, S. Hydrodynamics and Mass Transfer of Gas-Liquid and Liquid-Liquid Taylor Flow in Microchannels. *Chem. Eng. Technol.* **2017**, *40*, 1985–1998. [\[CrossRef\]](#)
15. Gascon, J.; van Ommen, J.R.; Moulijn, J.A.; Kapteijn, F. Structuring catalyst and reactor—An inviting avenue to process intensification. *Catal. Sci. Technol.* **2015**, *5*, 807–817. [\[CrossRef\]](#)
16. Kreutzer, M.T.; Bakker, J.J.W.; Kapteijn, F.; Moulijn, J.A.; Verheijen, P.J.T. Scaling-up Multiphase Monolith Reactors: Linking Residence Time Distribution and Feed Maldistribution. *Ind. Eng. Chem. Res.* **2005**, *44*, 4898–4913. [\[CrossRef\]](#)
17. Huerre, A.; Miralles, V.; Jullien, M.C. Bubbles and foams in microfluidics. *Soft Matter* **2014**, *10*, 6888–6902. [\[CrossRef\]](#) [\[PubMed\]](#)
18. Fu, T.; Ma, Y. Bubble formation and breakup dynamics in microfluidic devices: A review. *Chem. Eng. Sci.* **2015**, *135*, 343–372. [\[CrossRef\]](#)
19. Ładosz, A.; von Rohr, P.R. Pressure drop of two-phase liquid-liquid slug flow in square microchannels. *Chem. Eng. Sci.* **2018**, *191*, 398–409. [\[CrossRef\]](#)
20. Schubert, M.; Kost, S.; Lange, R.; Salmi, T.; Haase, S.; Hampel, U. Maldistribution susceptibility of monolith reactors: Case study of glucose hydrogenation performance. *AIChE J.* **2016**, *62*, 4346–4364. [\[CrossRef\]](#)
21. Abiev, R. Analysis of local pressure gradient inversion and form of bubbles in Taylor flow in microchannels. *Chem. Eng. Sci.* **2017**, *174*, 403–412. [\[CrossRef\]](#)
22. Jose, B.M.; Cubaud, T. Formation and dynamics of partially wetting droplets in square microchannels. *RSC Adv.* **2014**, *4*, 14962–14970. [\[CrossRef\]](#)
23. Helmers, T. On the Excess Velocity of Taylor-Droplets in Square Microchannels. Ph.D. Thesis, University of Bremen, Bremen, Germany, 2019.
24. Mießner, U.; Helmers, T.; Lindken, R.; Westerweel, J. An analytical interface shape approximation of microscopic Taylor flows. *Exp. Fluids* **2019**, *60*, 75. [\[CrossRef\]](#)
25. Helmers, T.; Kemper, P.; Thöming, J.; Mießner, U. Determining the flow-related cap deformation of Taylor droplets at low Ca numbers using ensemble-averaged high-speed images. *Exp. Fluids* **2019**, *60*, 66. [\[CrossRef\]](#)
26. Direito, F.; Campos, J.; Miranda, J.M. A Taylor drop rising in a liquid co-current flow. *Int. J. Multiph. Flow* **2017**, *96*, 134–143. [\[CrossRef\]](#)
27. Shams, M.; Raeini, A.Q.; Blunt, M.J.; Bijeljic, B. A study to investigate viscous coupling effects on the hydraulic conductance of fluid layers in two-phase flow at the pore level. *J. Colloid Interface Sci.* **2018**, *522*, 299–310. [\[CrossRef\]](#)
28. Ohnesorge, W.V. Die Bildung von Tropfen an Düsen und die Auflösung flüssiger Strahlen. *J. Appl. Math. Mech.* **1936**, *16*, 355–358. [\[CrossRef\]](#)
29. Wong, H.; Radke, C.J.; Morris, S. The motion of long bubbles in polygonal capillaries. Part 2. Drag, fluid pressure and fluid flow. *J. Fluid Mech.* **1995**, *292*, 95. [\[CrossRef\]](#)
30. Rao, S.S.; Wong, H. The motion of long drops in rectangular microchannels at low capillary numbers. *J. Fluid Mech.* **2018**, *852*, 60–104. [\[CrossRef\]](#)
31. Jakiela, S.; Makulska, S.; Korczyk, P.M.; Garstecki, P. Speed of flow of individual droplets in microfluidic channels as a function of the capillary number, volume of droplets and contrast of viscosities. *Lab Chip* **2011**, *11*, 3603–3608. [\[CrossRef\]](#)
32. Kalantarifard, A.; Saateh, A.; Elbuken, C. Label-Free Sensing in Microdroplet-Based Microfluidic Systems. *Chemosensors* **2018**, *6*, 23. [\[CrossRef\]](#)
33. Liu, H.; Vandu, C.O.; Krishna, R. Hydrodynamics of Taylor Flow in Vertical Capillaries: Flow Regimes, Bubble Rise Velocity, Liquid Slug Length, and Pressure Drop. *Ind. Eng. Chem. Res.* **2005**, *44*, 4884–4897. [\[CrossRef\]](#)
34. Howard, J.A.; Walsh, P.A. Review and extensions to film thickness and relative bubble drift velocity prediction methods in laminar Taylor or slug flows. *Int. J. Multiph. Flow* **2013**, *55*, 32–42. [\[CrossRef\]](#)
35. Angeli, P.; Gavrilidis, A. Hydrodynamics of Taylor flow in small channels: A Review. *Proc. Inst. Mech. Eng. Part C* **2008**, *222*, 737–751. [\[CrossRef\]](#)
36. Abadie, T.; Aubin, J.; Legendre, D.; Xuereb, C. Hydrodynamics of gas-liquid Taylor flow in rectangular microchannels. *Microfluid. Nanofluid.* **2012**, *12*, 355–369. [\[CrossRef\]](#)
37. Bretherton, F.P. The motion of long bubbles in tubes. *J. Fluid Mech.* **1961**, *10*, 166–188. [\[CrossRef\]](#)

38. Rocha, L.; Miranda, J.; Campos, J. Wide Range Simulation Study of Taylor Bubbles in Circular Milli and Microchannels. *Micromachines* **2017**, *8*, 154. [[CrossRef](#)]
39. Hantos, K.M.; Cameron, I.T. (Eds.) *Process Modelling and Model Analysis*; Academic Press: San Diego, CA, USA, 2001; Volume 4.
40. Han, Y.; Shikazono, N. Measurement of liquid film thickness in micro square channel. *Int. J. Multiph. Flow* **2009**, *35*, 896–903. [[CrossRef](#)]
41. Kreutzer, M.T.; Shah, M.S.; Parthiban, P.; Khan, S.A. Evolution of nonconformal Landau-Levich-Bretherton films of partially wetting liquids. *Phys. Rev. Fluids* **2018**, *3*, 42. [[CrossRef](#)]
42. Khodaparast, S.; Atasi, O.; Deblais, A.; Scheid, B.; Stone, H.A. Dewetting of Thin Liquid Films Surrounding Air Bubbles in Microchannels. *Langmuir* **2018**, *34*, 1363–1370. [[CrossRef](#)]
43. Morini, G.L. Viscous heating in liquid flows in micro-channels. *Int. J. Heat Mass Transf.* **2005**, *48*, 3637–3647. [[CrossRef](#)]
44. Abate, A.R.; Mary, P.; van Steijn, V.; Weitz, D.A. Experimental validation of plugging during drop formation in a T-junction. *Lab Chip* **2012**, *12*, 1516–1521. [[CrossRef](#)]
45. Musterd, M.; van Steijn, V.; Kleijn, C.R.; Kreutzer, M.T. Calculating the volume of elongated bubbles and droplets in microchannels from a top view image. *RSC Adv.* **2015**, *5*, 16042–16049. [[CrossRef](#)]
46. Bruus, H. *Theoretical Microfluidics*; Oxford University Press: Oxford, UK, 2008; Volume 18, p. 76.
47. Ransohoff, T.; Radke, C. Laminar flow of a wetting liquid along the corners of a predominantly gas-occupied noncircular pore. *J. Colloid Interface Sci.* **1988**, *121*, 392–401. [[CrossRef](#)]
48. Kreutzer, M.T.; Kapteijn, F.; Moulijn, J.A.; Kleijn, C.R.; Heiszwolf, J.J. Inertial and interfacial effects on pressure drop of Taylor flow in capillaries. *AIChE J.* **2005**, *51*, 2428–2440. [[CrossRef](#)]
49. Whitley, D. A genetic algorithm tutorial. *Stat. Comput.* **1994**, *4*. [[CrossRef](#)]
50. Davey, K.R. Latin Hypercube Sampling and Pattern Search in Magnetic Field Optimization Problems. *IEEE Trans. Magn.* **2008**, *44*, 974–977. [[CrossRef](#)]
51. Helmers, T.; Thöming, J.; Mießner, U. Retrieving accurate temporal and spatial information about Taylor slug flows from non-invasive NIR photometry measurements. *Exp. Fluids* **2017**, *58*, 66. [[CrossRef](#)]
52. Fuerstman, M.J.; Lai, A.; Thurlow, M.E.; Shevkoplyas, S.S.; Stone, H.A.; Whitesides, G.M. The pressure drop along rectangular microchannels containing bubbles. *Lab Chip* **2007**, *7*, 1479–1489. [[CrossRef](#)] [[PubMed](#)]
53. Jakiela, S.; Korczyk, P.M.; Makulska, S.; Cybulski, O.; Garstecki, P. Discontinuous transition in a laminar fluid flow: A change of flow topology inside a droplet moving in a micron-size channel. *Phys. Rev. Lett.* **2012**, *108*, 134501. [[CrossRef](#)] [[PubMed](#)]
54. Kumari, S.; Kumar, N.; Gupta, R. Flow and heat transfer in slug flow in microchannels: Effect of bubble volume. *Int. J. Heat Mass Transf.* **2019**, *129*, 812–826. [[CrossRef](#)]
55. Celata, G.P.; Morini, G.L.; Marconi, V.; McPhail, S.J.; Zummo, G. Using viscous heating to determine the friction factor in microchannels—An experimental validation. *Exp. Therm. Fluid Sci.* **2006**, *30*, 725–731. [[CrossRef](#)]

